Heritage Science

RESEARCH

Open Access

Corrosion of glaze in the marine environment: study on the green-glazed pottery from the Southern Song "Nanhai I" shipwreck (1127–1279 A.D.)

Benyuan Zhou[1], Qinglin Ma[2], Zhimin Li[2*], Zhiguo Zhang[3] and Naisheng Li[3]

Abstract

The "Nanhai I" shipwreck is an important discovery in the underwater archaeology of China, and many ceramics have been unearthed. These ceramics are important material artifacts of China's "Maritime Silk Road" and have considerable significance for the study of foreign trade in the Southern Song Dynasty (1127–1279 A.D.). However, these ceramics have been buried in a marine environment for approximately 800 years and have all been corroded to varying degrees, with green-glazed pottery being the most severely corroded. In this study, the chemical compositions of five samples of green-glazed pottery and the corrosion morphology and mechanism of a representative sample were analyzed by optical microscopy, scanning electron microscopy-energy dispersive X-ray spectrometry (SEM–EDS), Raman spectroscopy, and X-ray diffraction (XRD). Results: The green glaze is a low-temperature silica-aluminum oxide-lead oxide (SiO_2-Al_2O_3-PbO) glaze with copper ions (Cu^{2+}) as the main colorant. The corrosion morphology is characterized by alternating silicon (Si)- and lead (Pb)-rich layers, a sharp reaction interface between the Si-rich layer and the pristine glaze, and a relatively high porosity of the Si-rich gel layer, which is formed by the accumulation of spherical hydrated silica colloidal particles. These features suggest that the glaze was corroded through an interface-coupled dissolution–precipitation mechanism and that the properties of the gel pores controlled the reaction kinetics. Fluctuations in the solution properties at the reaction interface produced the complex morphology of the gel layer, whereas changes in the dryness and humidity of the environment are not essential factors. The samples have been corroding in the marine environment for nearly a thousand years, and explorations of the corrosion morphology and mechanism could provide reference information on the corrosion of various ancient ceramics and glasses and a basis for scientific conservation of these objects.

Keywords "Nanhai I" shipwreck, Ancient Chinese ceramics, Lead silicate glaze, Corrosion

Introduction

The "Nanhai I" shipwreck refers to an ancient ship in the Southern Song Dynasty that may have sailed from China to Southeast Asia or the Middle East to carry out overseas trade. The "Nanhai I" shipwreck was accidentally discovered on the seabed in 1987, approximately 20 nautical miles south of Dongping Port in Yangjiang City, Guangdong Province, China, and was overall salvaged and placed in the Yangjiang Maritime Silk Road Museum in 2007. The first formal comprehensive archaeological

*Correspondence:
Zhimin Li
lizhimin888@sdu.edu.cn
[1] Institute for Cultural Heritage and History of Science and Technology, University of Science and Technology Beijing, Beijing 100083, China
[2] International Joint Research Laboratory of Environmental and Social Archaeology, Shandong University, Qingdao 266237, Shandong, China
[3] National Centre for Archaeology, Beijing 100013, China

excavation of the wreck began in 2014, resulting in the recovery of many cultural relics. As of 2019, more than 180,000 exquisite cultural relics have been unearthed from this ancient shipwreck, among which ceramics and ironware constituted the largest proportion [1]. The ceramics mainly include celadon, bluish-white porcelain, black sauce-glazed porcelain, and green-glazed pottery. The ceramic forms include pots, bottles, jars, bowls, plates, dishes, powder boxes, and furnaces, covering almost all the varieties of porcelain produced by the main export porcelain kilns of the Southern Song Dynasty [2]. Long-term immersion in seawater, sedimentation and coverage by marine organisms have considerably damaged these unearthed ceramics. In particular, the green-glazed pottery has completely lost the original color of the glaze surface and has been severely corroded.

In the history of Chinese ceramics, low-temperature glazes containing lead (Pb) as a flux and metal oxides as colorants appeared as early as the Warring States Period (475-221 B.C.) [3]. These glazes were yellow, green, black, and brown, with green glazes based on copper oxide coloring being the most popular in the Middle and Late Eastern Han Dynasty (25–220 A.D.) [4, 5]. Many wares with Pb-green glazes have been unearthed in the tombs of the Eastern Han Dynasty in Henan and Shaanxi. With an elegant shape, a gorgeous color, and vivid decoration, this kind of pottery has both high artistic value and considerable historical and scientific value. The unearthed Pb-glazed pottery of the "Nanhai I" shipwreck provides important material evidence of trade and cultural exchanges between the ancient civilizations of the East and the West during the Southern Song Dynasty. Therefore, it is especially necessary and urgent to study how these green-glazed wares can be protected.

Ancient pottery with low-temperature Pb glazes has low corrosion resistance and therefore often has a bright surface sheen, called a "silvery glaze", that easily attracts attention. The extant poems of Emperor Qianlong (1711–1799 A.D.) on ancient pottery include a poem about a green-glazed pot from the Han Dynasty (202 B.C.-220 A.D.), i.e., "the green glaze is chapped around the body, the color is an external expression but the internal essence is pure, the damaged object with many defects is not the pristine subject, and if there is no dryness and wetness, there is no damage". ("斓斑青緑周身皴,光匪外发内蕴真。" "苦窳鬶垦非所论,燥湿弗受剥弗损。") This verse indicates that as early as the eighteenth century, the Qianlong Emperor had an intuitive awareness of the phenomenon of corrosion and the mechanism of damage to the surface of the green glaze. At the beginning of the twentieth century, Laufer [6], Hobson [7] researched Chinese ceramics, and all observed silvery glazes and rainbow phenomena on the surfaces of green-glazed pottery. However, this phenomenon was mistaken for metal precipitates deliberately applied to create a white glaze. Jackson [8] used modern techniques to analyze this material layer and found that the layer was a nonhomogeneous multilayered mixture. However, technological limitations prevented a clear determination of the materials and structures of this layer. In the 1960s, Tadashi Naito [9] and Ye [10] found that this layer had physical properties similar to those of mica. In the 1980s, the development of chemical analyses enabled scholars to gain a more accurate and in-depth understanding of the corrosion products and mechanisms of ancient lead glaze [11–20]. These studies indicated that the Pb ions in the ancient lead glaze mainly leach out of the solution through ion exchange and then combine with anions (e.g., CO_3^{2-}, SO_4^{2-}, S^{2-}, and Cl^-) in the solution to deposit on the glaze surface in the form of poorly soluble crystals. The leaching of Pb ions is accompanied by the formation of an amorphous Si-rich layer on the surface of the glaze. During the dehydration process, the silicate network in the Si-rich layer re-polymerizes and reorganizes in situ. Repeated wetting and drying cycles over a long period of time result in the formation of multilayered incrustation, giving the glaze an iridescent appearance.

The rainbow phenomenon is very common in the natural corrosion of silicate glass. Numerous studies have shown that the distinctive feature of the rainbow region is its fine laminated structure [21–24]. It is worth noting that the surface of the glass, whether buried in a stable underwater environment [22, 25–28] or soaked in a laboratory environment [29, 30] where there are no periodic changes in the physico-chemical conditions, always forms a multilayered incrustation. This shows that the corrosion process is spontaneous and influenced by the kinetics of an internal reaction between the solid and the solution. Lead glaze is a type of silicate glass. It is therefore necessary to question the mechanism of the corrosion of the ancient lead glazes as described above. The long-established model of glass corrosion proposes that the surface alteration layers are formed by solid-state diffusion of protons from solution into the glass, where they form silanol groups by exchange with mobile cations diffusing out of the glass. The product is a chemically modified residual glass that, in the solid state, eventually reconstitutes itself into a porous gel layer by condensation of the silanol groups [31–38]. In the last few years, the traditional view has been questioned by results from atomic probe tomography and transmission electron microscopy [39–42], which show an atomically sharp interface between the glass and the surface alteration layer (SAL), and by results from stable isotope tracer experiments [43–45], which show that the SAL must have precipitated from solution. These phenomena can be better explained by the new mechanism of "interface-coupled

dissolution–precipitation (ICDP)", which was proposed in the early twenty-first century in the study of corrosion of silicate minerals and glasses [43, 46–48]. In the ICDP model, the surface alteration layer (SAL) forms as a result of congruent (stoichiometric) dissolution of the glass, which is spatially and temporally coupled with precipitation of amorphous silica at an inward moving reaction front. Such a replacement reaction is driven by the difference in solubility between silicate glass and amorphous silica from a thermodynamic point of view. Since thermodynamic equilibrium between glass and solution is never reached, the reaction is not reversible. Thus, in an inward-moving dissolution-deposition front, an increasing amount of amorphous silica can replace glass. Recently, the ICDP model has been extended to include an ion exchange zone that can develop ahead of an ICDP front if the dissolution–precipitation rate is dramatically slowed [45]. This self-organization coupling of these reactions may be the key to understanding the formation of laminar or more complex structural and chemical patterns observed in natural corrosion zones of ancient Pb glazes.

The surface of the green-glazed pottery from the Nanhai I shipwreck has been severely corroded. To find a means of protecting this type of pottery, detailed analyses of the chemical compositions, physical compositions and microscopic morphologies of the corrosion products on the surface of the green glaze were performed in this study, and the process and mechanism for glaze formation were elucidated. The layered deposits in the corrosion products of the Pb-green glaze are mostly considered to be the products of alternating wet and dry environments. The Pb-green glaze samples investigated in this study were buried in a relatively stable marine environment for approximately 800 years, and studies of the corrosion morphology and formation mechanism of the corrosion products on these samples could improve our understanding of ancient Pb-glaze corrosion and provide reference information for studies of the long-term corrosion mechanisms of modern silicate glasses.

Materials

Analytical techniques

Optical microscopy (OM) The macroscale morphology of the glaze surfaces and polished cross-sections were observed with an ultra-depth of field 3D microscope (Keyence VHX-6000).

Scanning electron microscopy–energy dispersive X-ray spectrometry (SEM–EDS) The micromorphology and micro-area chemical compositions were characterized using SEM (Thermo Scientific, Quattro S) with a Bruker QUANTAX EDS X-ray spectrometer. The analyses were carried out in a low vacuum (60 Pa) environment with an operating voltage of 15 kV and element acquisition at a working distance of 10 mm for 30 s, with P/B-ZAF for stoichiometric quantification. To observe the sample cross-sectional microstructure, small pieces of approximately 1 cm^3 were cut at the edges of the sample using a diamond saw blade, embedded in epoxy resin, and later polished using SiC sandpaper and diamond polishing paste (3 μm, 1 μm).

Micro-Raman The phase components of the glaze were characterized using a laser micro-confocal Raman spectroscopy (RENISHAW inVia). It was equipped with a research-grade Leica microscope with a spatial resolution of < 0.5 μm. Optical lenses were 50 × and 100x, and laser wavelength was 785 nm. The laser power on the samples was 2.8 mW.

The baseline was subtracted using WiRE 4 software. The WiRE™ (Windows -based Raman environment) software from Renishaw features a patented Intelligent Fitting baseline subtraction tool that can be used to automatically and accurately eliminate unwanted backgrounds from spectra, and this automated background removal makes removal more consistent between similar spectra [49]. The Raman spectrum of the pristine glaze and corroded glaze were deconvoluted using Origin software peak-fitting module (Microcal Software, Inc.), and a gaussian shape was assumed for all Raman lines because of the disordered state of examined materials. We set the number of expected components (e.g. five for the stretching envelope) and assumed that all bands parameters (frequency, half-width and intensity) are independent and unconstrained.

X-ray diffraction (XRD) The crystal phases of the glaze were determined by XRD (PANalytical Aeris benchtop X-ray diffractometer) with Cu Ka radiation (40 kV and 40 mA) and 2θ ranged from 10° to 70°. The sample surface corrosion products were scraped, ground to a fine powder in an agate mortar and then applied to a single crystal silicon sample holder and fed into the X-ray diffractometer for testing.

Green-glazed pottery samples

The samples are shown in Fig. 1. All of samples are stamped disc remnants, with an embossed flower pattern on the mouth edge and inner bottom, a diamond-shaped mouth, flat folded edge, shallow arc belly, flat bottom, and the entire body is glazed. The samples are blue-gray body with a green glaze. Archaeological findings regarding the shapes and decoration patterns of the samples have led scholars to identify green-glazed pottery samples as exported products of the Fujian Cizao kiln complex from the Song Dynasty [50]. The five pieces of green-glazed pottery tested here had undergone a desalination process by immersion in deionised water and were kept in a dry,

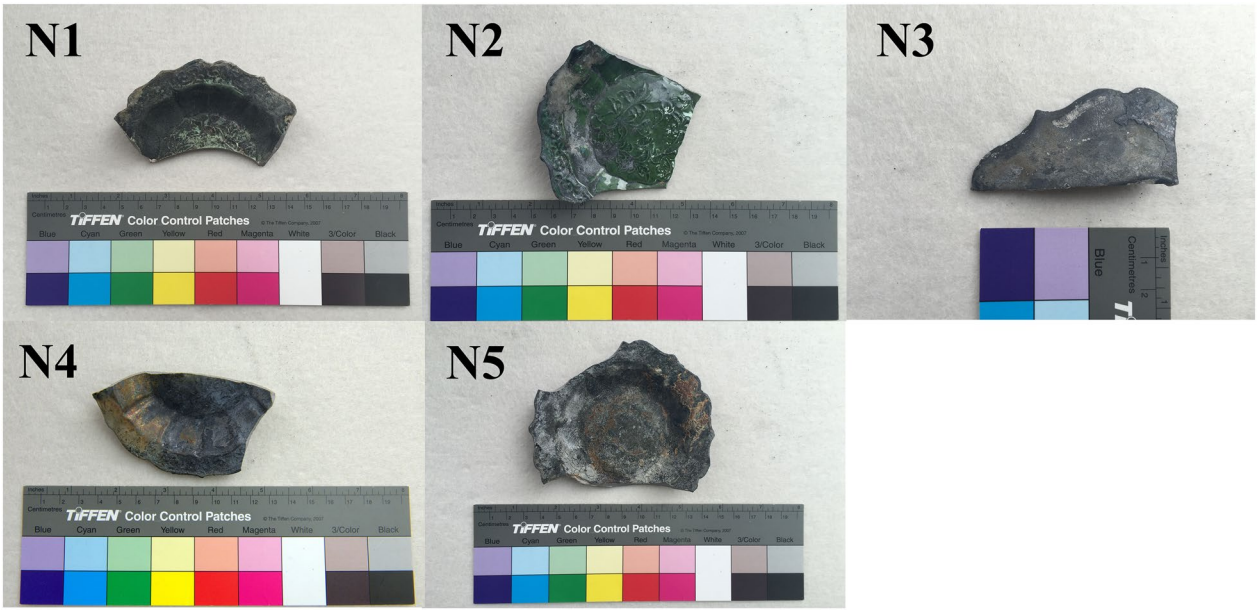

Fig. 1 Photographs of green-glazed pottery sherds from the "Nanhai I"

sheltered and light-proof storage room after the desalination was completed. The relative humidity of the storehouse was maintained at 35–65% throughout the year. The samples were numbered from N1 to N5. Corrosion has significantly changed the color of the glaze, and some areas have turned black and yellow.

Results and analyses

Chemical compositions of the pristine glazes

The corrosion study of the glaze was based on an analyses of the chemical compositions of the pristine glazes of the samples. Table 1 shows the SEM–EDS results for the chemical composition of the glaze in an uncorroded area of a sample cross-section. Based on the chemical composition, the green glaze of all five pieces is identified as a silica-aluminum oxide-lead oxide (SiO_2-Al_2O_3-PbO) low-temperature glaze, with Pb^{2+} as the main flux and divalent copper ions (Cu^{2+}) as the main colorant.

Different structures can cause the Pb glaze to react differently under an external medium. A Pb glaze contains two different structural forms of Pb: Si–O–Pb bonds (where O denotes oxygen) that act as network modifiers, and Pb–O-Pb bonds that act as network formers. At low Pb concentrations (PbO < 40 mol%), the structure of PbO-SiO_2 glass is close to that of an alkali silicate glass, and Pb acts as a network modifier. At high Pb concentrations (PbO > 60 mol%), Pb exists in the form of a PbO_n (n = 3 and 4) polymer chain that forms a network. Irrespective of whether Pb acts a network former or modifier, Pb remains in a positive divalent redox state [51–53]. As the samples have a PbO content of 31–33 mol%, Pb acts as a network modifier in the glaze, which contains typical Si–O-Pb bonds. In these samples, CuO is the main colorant at a content of 3–5 mol%, and the iron oxide (Fe_2O_3) content is low at 0.5–0.6 mol%. In the Pb glaze, Cu^{2+} acts as a modifying ion and exists in an octahedral configuration in a glassy matrix. Compared to tetrahedral coordination (Fe), octahedral coordination has longer

Table 1 Pristine glaze chemical composition (Wt%)

Sample No	Na_2O	MgO	Al_2O3	SiO_2	K_2O	CaO	Fe_2O_3	CuO	PbO
N1	0.4	0.2	4.4	28.2	0.4	0.2	0.7	2.4	63.1
N2	0.3	0.1	5.2	30.7	0.3	0.3	0.7	2.2	60.2
N3	0.4	0.1	4.3	29.6	0.6	0.3	0.8	2.9	61.0
N4	0.4	0.1	4.3	28.9	0.5	0.3	0.8	3.8	60.9
N5	0.5	0.2	6.4	30.0	0.3	0.1	0.5	2.8	59.2

bond lengths and a larger effective volume, a more open cage structure, and places fewer geometric and energetic restrictions on ion movement and exchange (that is, the electron density and activation energy are lower) [54–56]. Therefore, green lead glazes with Cu^{2+} as the colorant are more susceptible to corrosion than yellow lead glazes with Fe^{3+} as the colorant.

Analysis of glaze corrosion morphology

Microscopic observations and compositional analyses show few differences in the chemical compositions and corrosion morphologies of the glazes in the five samples. In this study, Sample N4 was selected as a representative sample, and its corrosion process was analyzed in detail. The N4 corroded glaze is mainly golden yellow with local iridescence and black.

Corrosion morphology in the golden yellow area of glaze

The following results were obtained by optical microscopy (Fig. 2a) and SEM–EDS (Fig. 2c–f). The corrosion products in the golden crust area are distributed in layers: in the outermost golden crust (Additional file 1: Table S1-EDX8), the Fe_2O_3 content is 49 Wt%, and the sulfur trioxide (SO_3) content is relatively low, about 4 Wt%, so the material must be an iron oxide/hydroxide. Raman spectrum analyses indicates the presence of hematite (Fig. 2b). However, the illumination power of the laser beam is 2.8 mW, which generates high temperatures that may heat the low-valent iron oxides and iron

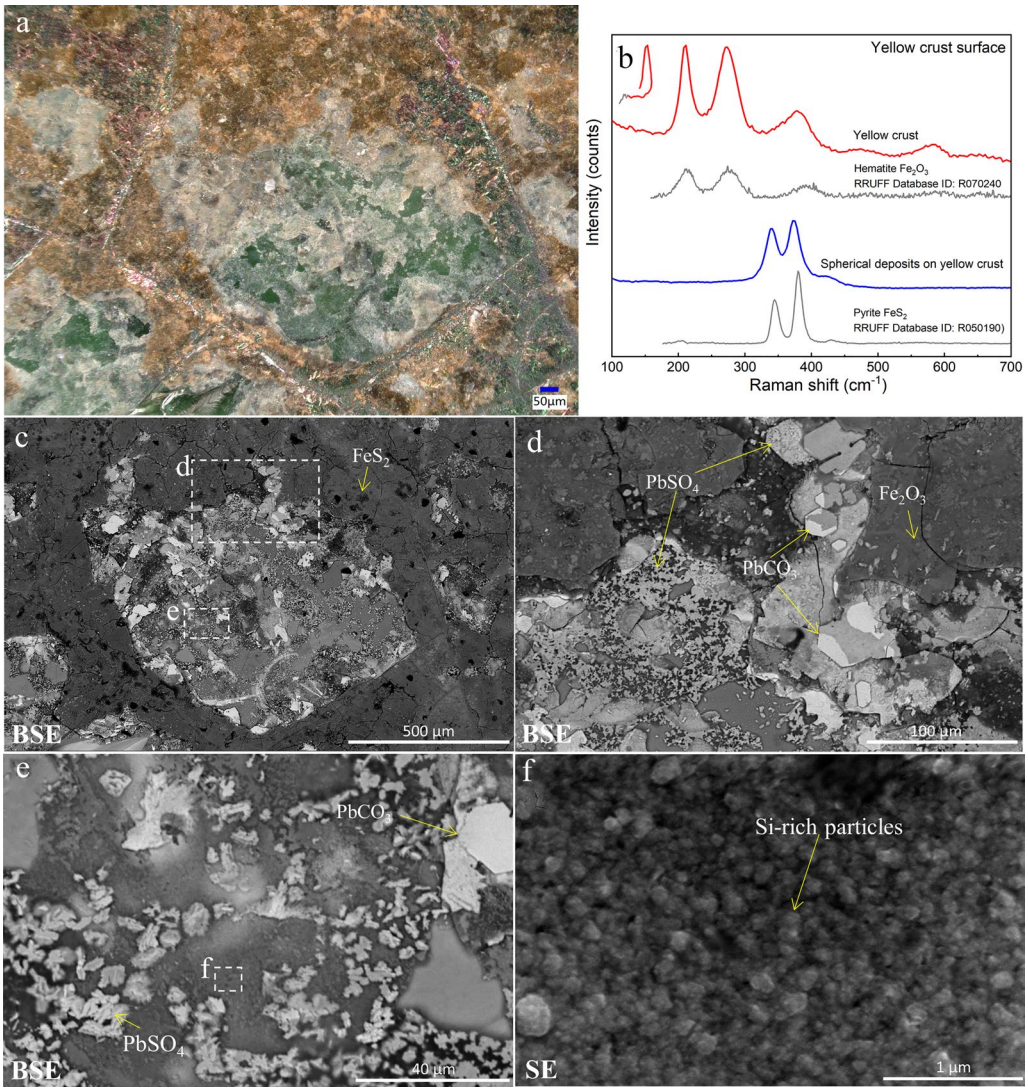

Fig. 2 Golden yellow area. **a** Optical micrograph; **b** Raman spectrum of golden yellow crust surface; **c–f** SEM images

hydroxides and transform them into hematite [57], so it is not certain that the material is definitely hematite. Nevertheless, the hematite in the surface crusts should be the main phase of the sample after it has been salvaged from the water and stored in the atmosphere for a long time. In the golden yellow crusts, spherical substances with high sulfur (S) and Fe contents are also observed, which are identified as authigenic microspheroidal pyrites (Fig. 2b, c, Additional file 1: Table S1-EDX1). There are white and yellowish corrosion products beneath the golden crust that are mainly short columnar lead sulfate ($PbSO_4$) crystals (Fig. 2d, e, Additional file 1: Table S1-EDX2, EDX5, EDX9) and hexagonal plate lead carbonate ($PbCO_3$), where the $PbCO_3$ crystals in local areas may have been infiltrated by surface Fe (Fig. 2d, Additional file 1: Table S1-EDX3, EDX4). The corrosion products in the golden crust area were scraped off and found to consist mainly of $PbCO_3$ and $PbSO_4$ by XRD analysis (Fig. 3). The inner corrosion layer appears translucent white and is identified by SEM–EDS analysis to consist of granular aggregates with a high Si contents (Fig. 2f, Additional file 1: Table S1-EDX10). This layer is referred to as a Si-rich (gel) layer in this paper and is discussed below.

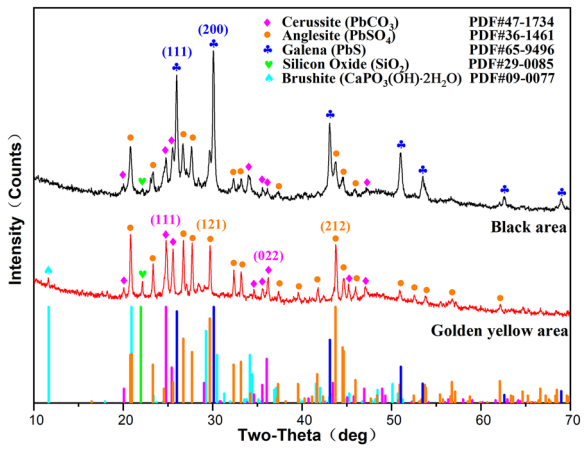

Fig. 3 XRD patterns for the corrosion products

The element line-scan image (Fig. 4c) for a cross-section of the golden crust shows wave-like opposing distributions for the Si and Pb contents and indicates that the sodium (Na) and potassium (K) contents are the most abundant elements in the innermost corrosion layer. The Fe content decreases linearly from the exterior to the interior, which presumably results from the diffusion of substances from the external environment into the corroded glaze layers. The Fe content is considerably

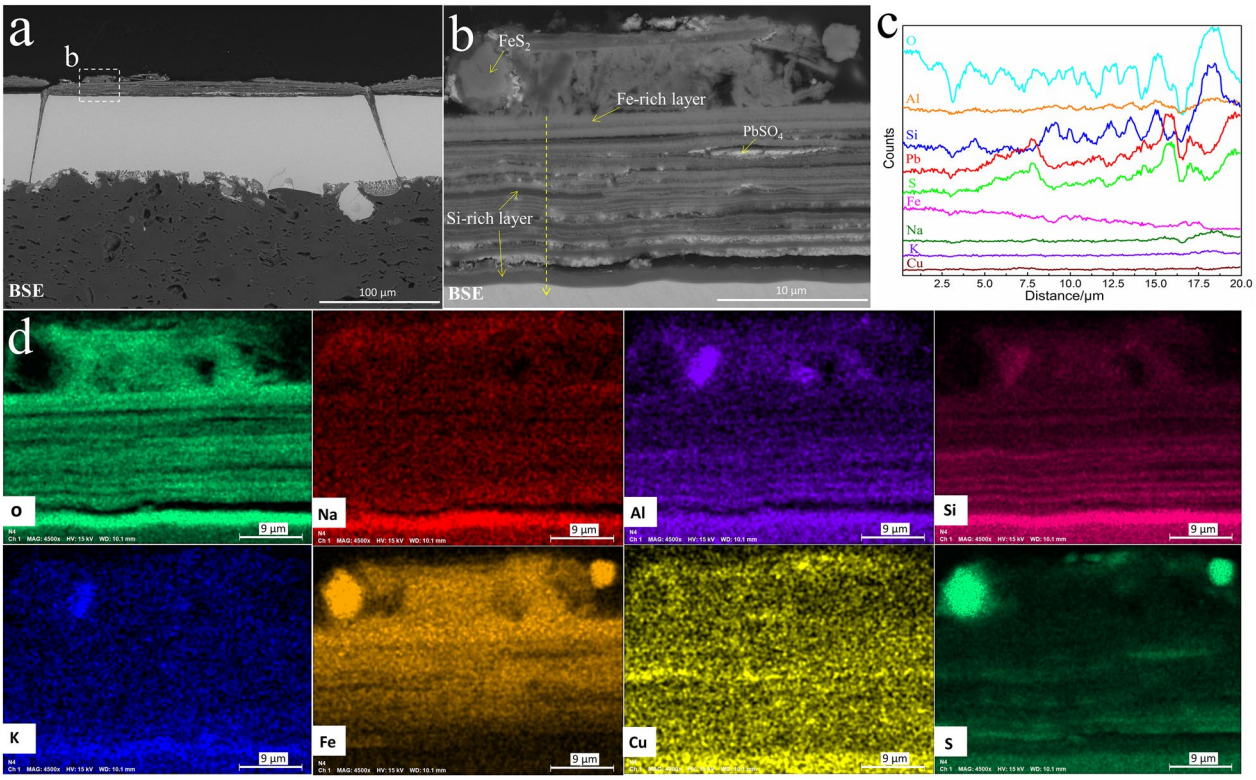

Fig. 4 **a, b** SEM images of the polished cross-section of golden yellow crust area; **c, d** SEM images of EDS element line-scan and the mapping images

higher in the outside layers (Fig. 4b, Additional file 1: Table S2-EDX1,EDX4) than in the inside layers (Fig. 4d). Thus, the outside layers are the Fe-rich layers of the corrosion layers with n(Fe)/n(Si) = 1.4 and n(Fe)/n(Si) = 1.5, respectively, and they have well-defined Si contents. The micrographs show many pores structures in the Fe-rich layer (Fig. 4b), presumably due to permeable deposits of Fe-rich minerals in the Si-rich gel layer. Interactions between the gel layer and the Fe-rich minerals could not be identified decisively in this study. Spherical particles are attached to the surface of the corrosion layer that consists mainly of elemental S and Fe (n(S):n(Fe) ≈ 2:1) and are authigenic microspheroidal pyrites (Fig. 4b, Additional file 1: Table S2-EDX3). The golden yellow color of the sample surface results from the deposition of hematite and pyrite.

Corrosion morphology in iridescence area of glaze

The local area under the golden-yellow crust on the glaze surface has various colorations. Optical microscopy reveals a colored stripe on a white base and various single colors, including dark blue, yellow, and silver-black (Fig. 5a). In the SEM micrographs, colored fringes appear on the Si-rich layer (Fig. 5c, Additional file 1: Table S3-EDX1), and the Pb-rich layer (Fig. 5c, Additional file 1: Table S3-EDX2) has a single color and is identified as $PbSO_4$ by Raman spectroscopy (Fig. 5b). Observation of a cross-section reveals that the Si-rich gel layer and Pb-rich layer are 200–900 nm in thickness (Fig. 4b), which covered the entire wavelength range of visible light. Irradiation of the film with white light produces a thin-film interference effect. The specific interference color is controlled by the optical path difference of the coherent light, which is related to the refractive index and thickness of the film. Colored stripes appear for a film with an uneven thickness. A film with a uniform thickness of ca.200 nm (which is half the wavelength of blue light) appears blue. In the silver-black area, tiny cubic crystals of galena can be observed embedded in the pores of the Si-rich layer (Fig. 5d, Additional file 1: Table S3-EDX4, EDX5). The galena exhibits a

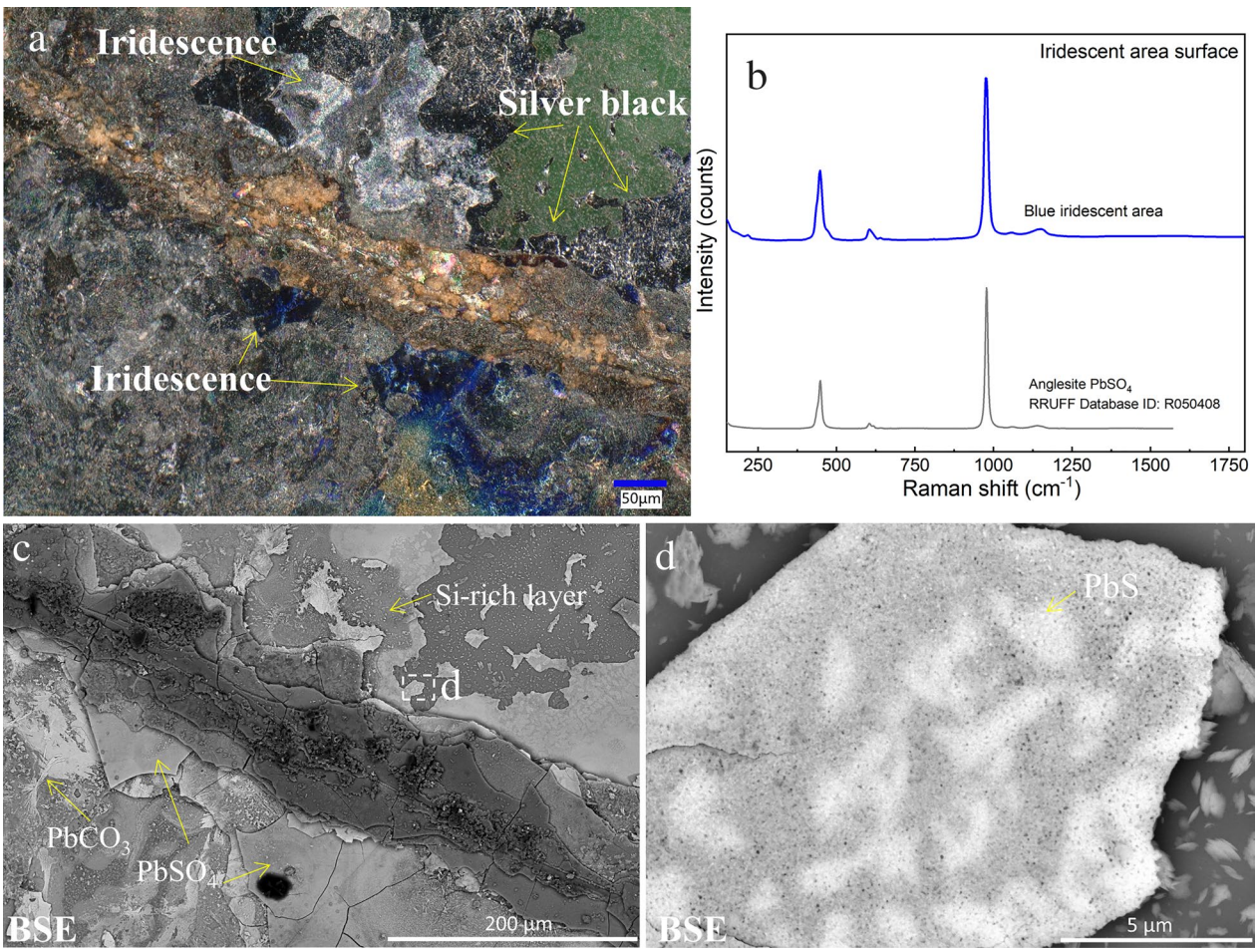

Fig. 5 Surface iridescent area **a** Optical micrograph; **b** Raman spectrum of blue iridescence area; **c, d** SEM–EDS images

lead-gray color with gray-black streaks, a metallic luster, and opaqueness. It is speculated that the silver-black area primarily contains a chemical colorant, which obscures the structural color produced by the thinness of the layer.

Corrosion morphology in the black area of glaze

The black crust area appears black overall under the optical microscope (Fig. 6a), has shed material in a scaly pattern, and the innermost local area is silvery white. The corrosion products in the black crust area were scraped and found to mainly contain galena, cerussite, and anglesite by XRD analysis (Fig. 3). The SEM micrograph reveals that the corrosion products in the surface layer (Fig. 6c, d) are arranged in a disorderly manner: there are small cubic particles mainly containing Pb and S, with n(Pb):n(S) ≈ 1:1 (Additional file 1: Table S4-EDX7), corresponding to galena; biconical dodecahedrons formed by the superposition of hexagonal thin plates mainly containing Cu and S, with n(Cu):n(S) ≈ 1:1 (Additional file 1: Table S4-EDX8), that are identified as covellite from the Raman spectrum (Fig. 6b); and columnar or plate-shaped aggregates mainly containing Pb, S, with n(Pb):n(S) ≈ 1:1 (Additional file 1: Table S4-EDX4), that are identified as anglesite from the Raman spectrum (Fig. 6b). Small particles, such as anorthite, albite, mica, and quartz, are also scattered through the surface layer (Additional file 1: Table S4-EDX1, EDX2, EDX3, EDX5).

Under the surface corrosion layer, flaky aggregates of cerussite (Fig. 7c,d) and columnar or plate-shaped aggregates of anglesite (Fig. 7a) grow vertically on the glaze surface, and many cubic crystals of galena (Fig. 7b) are scattered in the dark Si-rich matrix. The numerous crystals grown vertically on the glaze destroyed the layered structure, and the large galena content causes the corrosion glaze to appear black overall.

The inner corrosion layer (Fig. 8a–e) is itself layered and appears bright white under the optical microscope (Fig. 6a). The SEM micrographs show that the layered material is mainly composed of a bright layer and a dark layer. The dark layer has a relatively high content of SiO_2

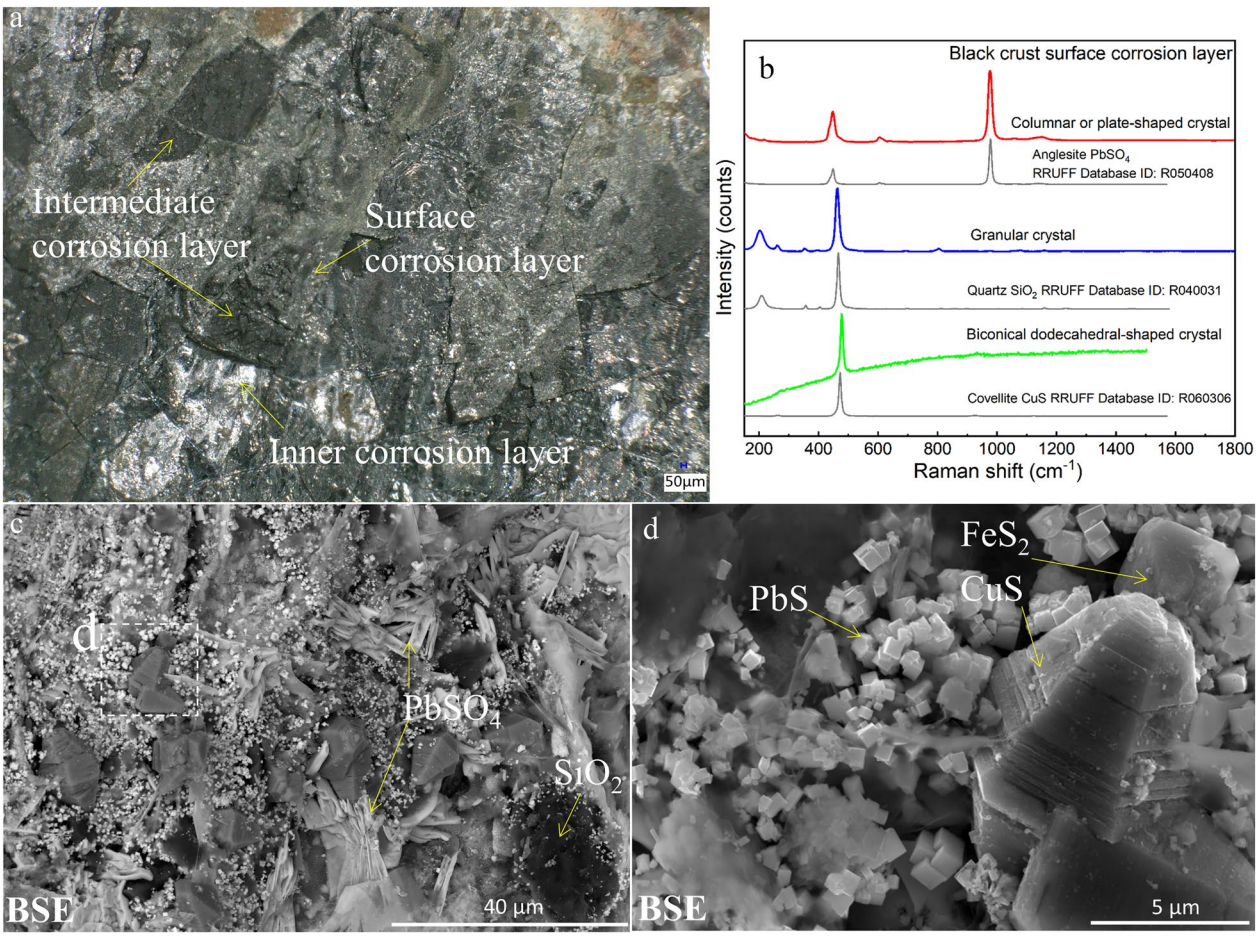

Fig. 6 **a** Optical micrograph of the glaze of the black crust area; **b** Raman spectrum of surface corrosion layer; **c, d** SEM images of the surface corrosion layer

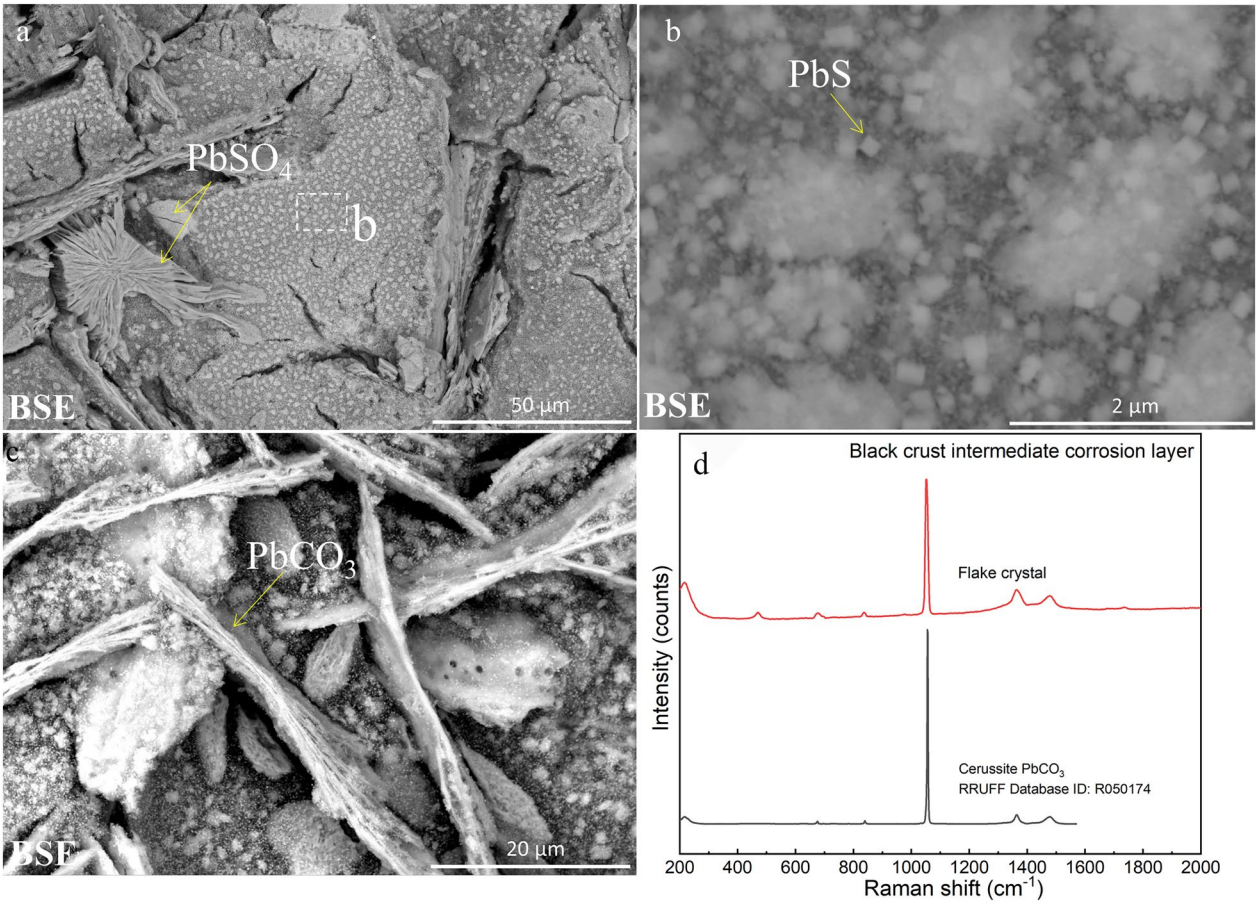

Fig. 7 Intermediate corrosion layer of the black crust area: **a–c** SEM images **d** Raman spectrum of the flaky aggregates

(Additional file 1: Table S4-EDX10) and is porous due to the agglomeration of granular substances with particle sizes of 50–150 nm. The pores between these particles are large, with sizes up to 500 nm in size. (Fig. 8c,d) The bright layer has a high PbO content, and many well-developed cubic crystals with sides measuring 1–2 μm are lying flat on the porous dark Si-rich layer (Fig. 8b). The plane structure and the surfaces of many crystals reflect light strongly, which is manifested as a bright silver color. Tetragonal and tetrahedral crystals with high contents of S, Fe, and Cu are also found, which are identified as chalcopyrite based on a Raman spectral analysis (Fig. 8e, f, Additional file 1: Table S4-EDX11).

The cross-section of the black area (Fig. 9, Additional file 1: Table S5) has a similar corrosion morphology to that of the surface: the inner layer consists of parallel layers of PbS crystals to the Si-rich layer. Flaky $PbCO_3$ crystals and columnar $PbSO_4$ crystals are irregularly distributed in the outer layer, disturbing the parallel structure of the corrosion layer. Under a polarized light microscope (Additional file 1: Fig.S6), galena, anglesite, and cerussite show different white, blue-green, and gray-white colors, respectively, which indicates the distributions of the corrosive minerals.

Analysis of Si-rich gel layer

Chemical composition of Si-rich gel

The corrosion layer in contact with the pristine glaze is a Si-rich layer, which is the corrosion reaction front. Therefore, it is essential to analyze the Si-rich layer in order to understand the corrosion mechanism. The glaze has multiple Si-rich layers. Compared to the composition of the pristine glaze shown in Fig. 10, the Si-rich layers have a significantly lower PbO contents, suggesting that lead was lost from the glaze to the marine solution during the formation of the Si-rich layer. The inner side Si-rich layer, which is the reaction frontier, contains most of the Na and K elements, and the outer side Si-rich layer contains more Fe and Ca. This suggests that the marine elements Na and K are directly involved in the formation of the Si-rich layer through chemical interactions, while the Fe and Ca elements are accumulated on the outer side Si-rich layer through physical interactions such as deposition.

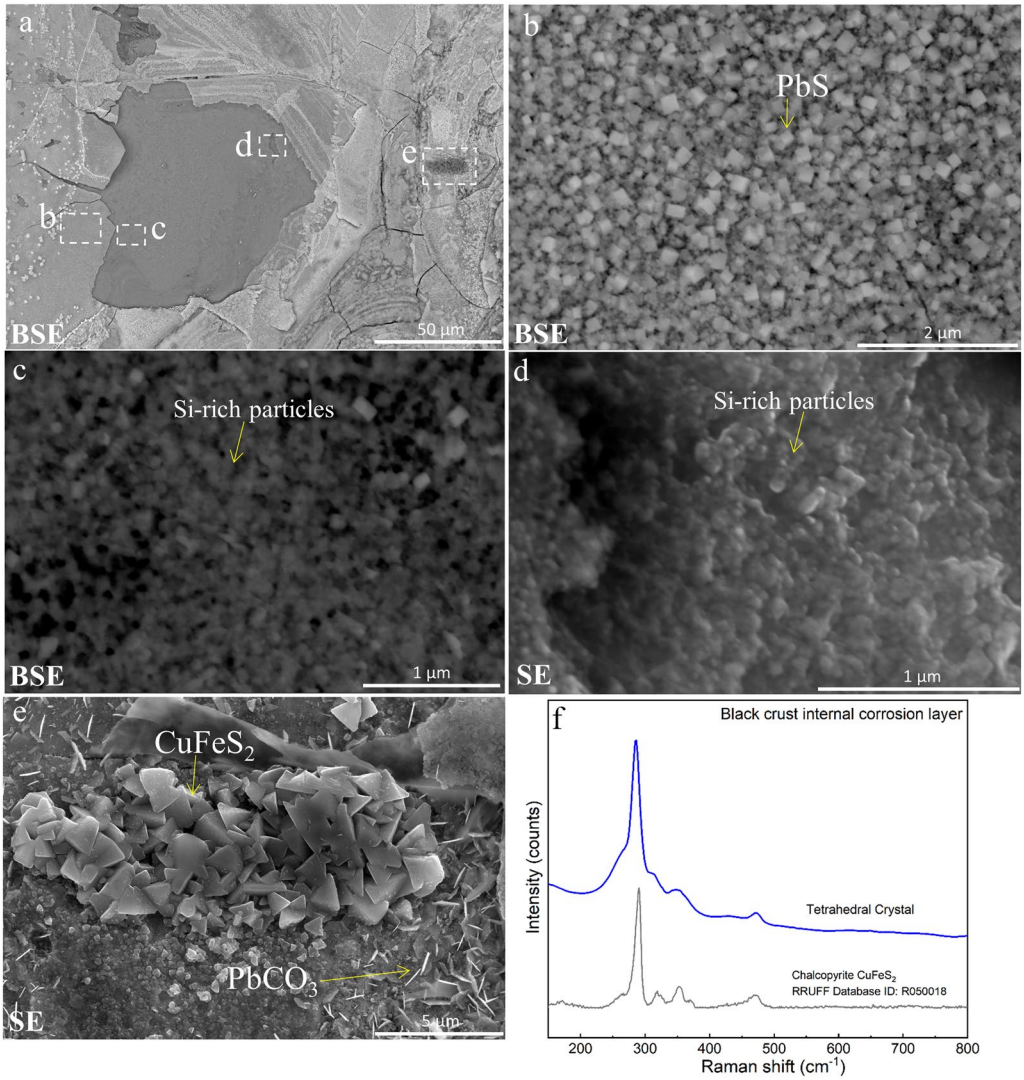

Fig. 8 Bottom corrosion layer of the black crust area: **a–e** SEM images; **f** Raman spectrum of the tetrahedral crystals

To analyze elemental migration between the pristine glaze and the Si-rich layer, SEM–EDS was used to obtain an elemental line distribution diagram (Fig. 11). The following content variations are shown in the diagram. The Si content reaches a maximum in the Si-rich layer and then decreases rapidly beyond this layer; the O content reaches a maximum in the Si-rich layer, gradually decreases and then stabilize at approximately 700 nm beyond this layer; the Pb content gradually increases and then stabilize at approximately 500 nm beyond the Si-rich layer; and the Na content gradually decreases until it stabilize at approximately 500 nm beyond the Si-rich layer. The trends for the changes in the O, Pb, and Na contents indicates diffusion of these elements, which may be related to the ion exchange reaction between Pb^{2+} in the glaze and hydronium (H_3O^+), hydrogen (H^+), and Na^+ ions in the solution and to the entry of water (H_2O) molecules into the glaze matrix. The Si-rich layer is approximately 1.6 μm thick, and it is speculated that a diffusion layer of approximately 700 nm is present between this layer and the pristine glaze, where hydration and ion exchange reactions take place. There is a clear variation in the Si content at the Si-rich layer boundary, indicating that the Si-rich layer and the pristine glaze layer are not connected due to the recondensation and deposition of the hydrolyzed Si–O framework.

Structure of Si-rich gel

Raman spectroscopy is used to analyze the structure of chemical bonds in materials. Even optically

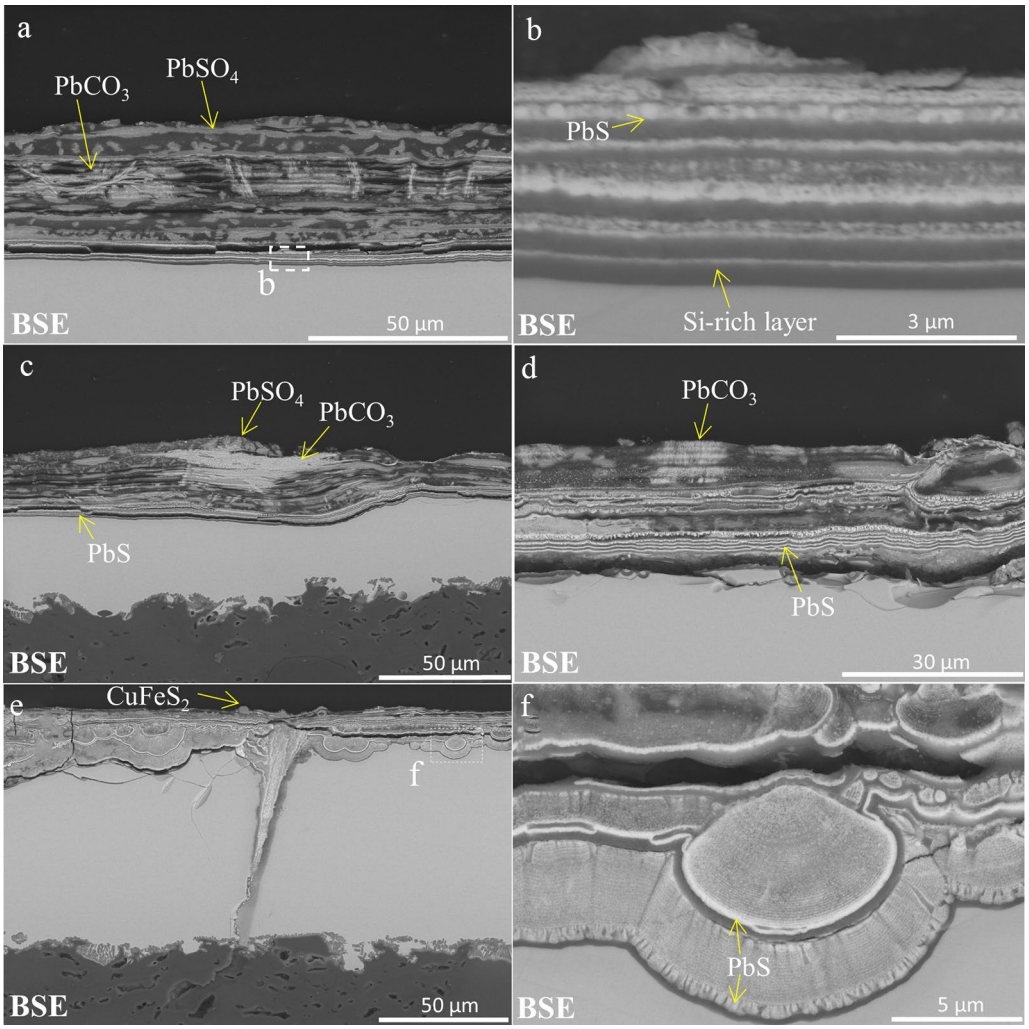

Fig. 9 SEM images of the polished cross-section of black crust area

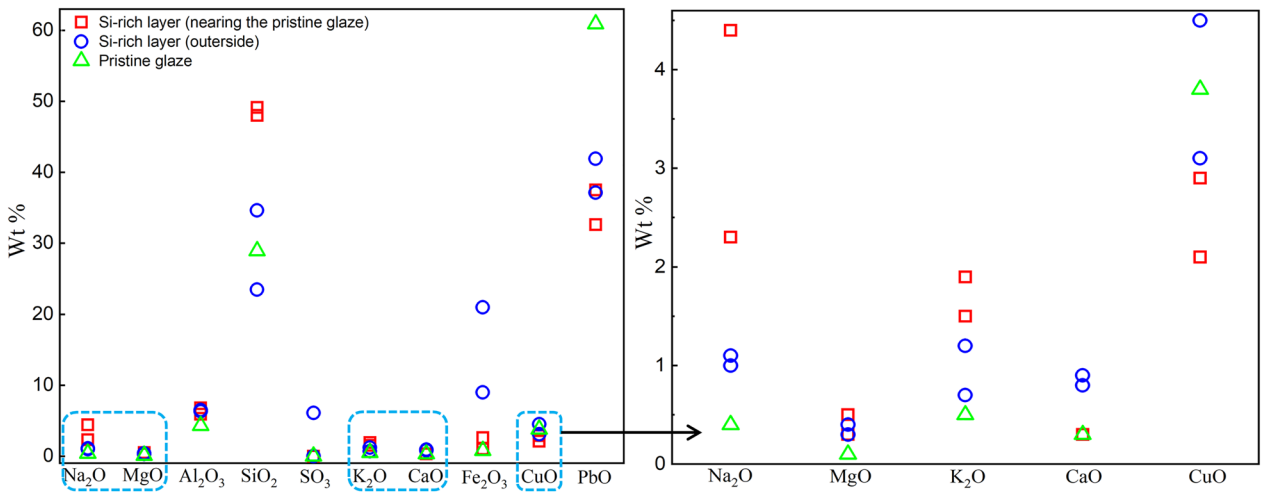

Fig. 10 Scatter plot of component distribution in pristine glaze, inner and outer Si-rich layers (Data from Table 1-N4; Additional file 1: Table S2-EDX6, EDX7; Additional file 1: Table S5-EDX2, EDX5)

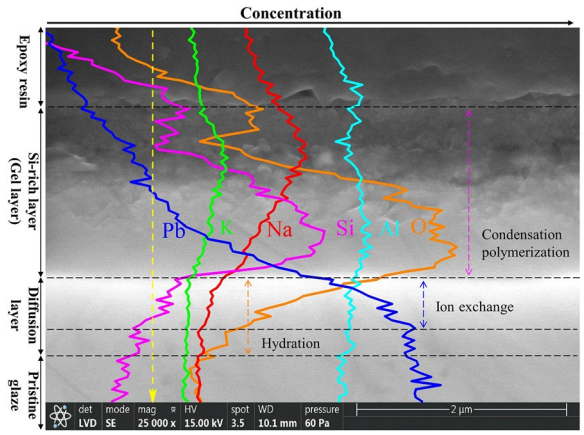

Fig. 11 EDS line-scan profile of the reaction interface

homogeneous glasses can present heterogeneity on the scale of SiO_4 structural units due to manufacturing process [58] or surface corrosion. Thus, the corrosion of the glass surface can be revealed by Raman spectroscopy. In Raman spectra of the Si-rich layer and the pristine glaze of the N4 sample (Fig. 12a, b), peaks appear at approximately 470 cm^{-1} and 950 cm^{-1}, respectively, which originate from the bending vibration and stretching vibration modes of the orthosilicate (SiO_4) tetrahedra, respectively. In highly connected structures, the larger the amplitude motion of oxygen perpendicular to the Si–O–Si link, the higher is the polarization change in this vibration and Raman intensity around 500 cm^{-1}. In less connected structure, the larger the amplitude motion of oxygen by a stretching mode, the larger is the Raman intensity at ca. 1000 cm^{-1} [59]. Therefore, the area ratio of the bending peak to the stretching peak (A_{470}/A_{950}) can be used to determine the degrees of polymerization in the Si-rich

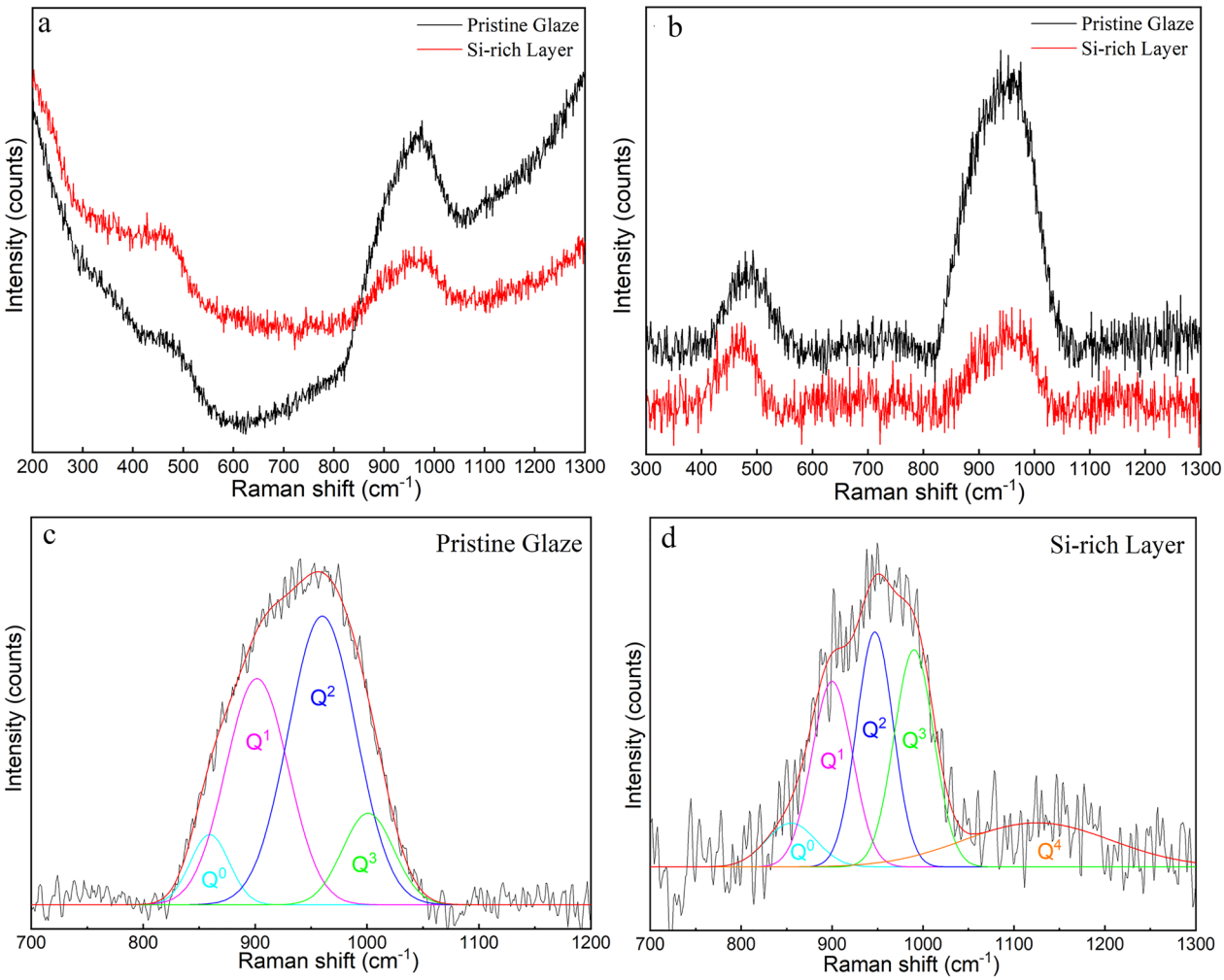

Fig. 12 Raman spectra of pristine glaze and Si-rich layer: **a** raw Raman spectrum; **b** Raman spectrum after background removal; **c** deconvolution of the Raman spectrum for the pristine glaze (800–1100 cm^{-1}); **d** deconvolution of the Raman spectrum for the Si-rich layer (800–1300 cm^{-1})

Table 2 The integral area ratios of the bending envelope to stretching envelope in the Raman spectra of the pristine glaze and the Si-rich layer (A_{470}/A_{950}) and the peak positions and integral area ratios of each component (Q^n) in the stretching envelope (A_{Q^n}/A_{950})

Regions	A_{470}/A_{950}	Parameters	Q^0	Q^1	Q^2	Q^3	Q^4
Pristine glaze	0.18	Peak position	859	902	960	1001	–
		A_{Q^n}/A_{950}	0.07	0.34	0.48	0.11	–
Si-rich layer	0.56	Peak position	855	900	955	995	1130
		A_{Q^n}/A_{950}	0.07	0.23	0.26	0.26	0.20

layer and the pristine glaze. For the N4 sample, $A_{470}/A_{950}=0.18$ in the pristine glaze, and $A_{470}/A_{950}=0.56$ in the Si-rich layer (Table 2), indicating a higher degree of polymerization (structural connectivity) in the Si-rich layer than in the pristine glaze. As the A_{470}/A_{950} ratio of the pristine glaze is low (less than 0.3), it is speculated that a low firing temperature was used to produce the N4 sample glaze [60].

Regarding the Si–O stretching vibrations of the SiO_4 tetrahedra, Raman peaks at approximately 830 cm^{-1}, 900 cm^{-1}, 960 cm^{-1}, 1000 cm^{-1}, and 1150 cm^{-1} have been reported in the literature for no, one, two, three, and four bridging oxygen atoms, respectively (denoted by Q^0 or isolated SiO_4, Q^1 or -SiO_3, Q^2 or =SiO_2, Q^3 or ≡SiO, and Q^4 or SiO_2, respectively) [61, 62]. The stretching vibrational peaks at 950 cm^{-1} in the spectra of the pristine glaze and Si-rich layer were fitted and deconvoluted (Fig. 12c, d, Table 2), indicating the proportions of the Q^1 and Q^2 components in the spectrum of the pristine glaze are relatively high, and slightly lower in the spectrum of the Si-rich layer. The proportions of Q^3 and Q^4 in the spectrum of the Si-rich layer are higher than those in the spectrum of the pristine glaze, indicating there are more bridging O bonds in the Si-rich layer than in the pristine glaze. Therefore, the Si-rich layer is speculated to be composed of SiO_2 nanocolloidal particles formed by polycondensation of silicic acid.

Discussion

Formation mechanism of corrosion products such as lead minerals and hematite

The "Nanhai I" shipwreck is located in the waters near Shangchuan Island and Xiachuan Island in Yangjiang, Guangdong, at a water depth of 22–24 m and an average burial depth of 1–3 m in a silt seabed. In the offshore area of western Guangdong where the shipwreck is located, the bottom seawater has average pHs of 8.22, 8.32, 8.28, and 8.21 in the spring, summer, autumn, and winter, respectively, and an average salinity of approximately 30.6‰ [50, 63]. Compared to the bottom seawater, the free water in the seabed sediment voids in the northern part of the South China Sea has a higher electrical conductivity and higher concentrations of hydrogen carbonate ions (HCO_3^-) [64]. In the seabed soil, the O_2 concentration is very low, and bacteria, such as anaerobic sulfate-reducing bacteria, grow and multiply. The SO_4^{2-} ion concentration in seawater is relatively high at an average concentration of 29 mmol/L, which is hundreds of times that in freshwater [65]. These SO_4^{2-} ions are present in large quantities and are the most important electron acceptors in seawater. In the presence of a sufficient quantity of organic matter in the seabed sediments, sulfate-reducing bacteria use SO_4^{2-} as an electron acceptor to metabolize small organic molecules to S^{2-}, where the reaction principle is shown in Eq. (1) [66]. Therefore, many anions, such as S^{2-}, SO_4^{2-}, and CO_3^{2-}, are present in the marine soil environment.

$$2(CH_2O) + SO_4^{2-} + 2H^+ \xrightarrow{\text{sulfate reducing bacteria}} H_2S + 2H_2O + CO_2 \quad (1)$$

The samples have a PbO content of approximately 60 wt%, and Pb occurs as a network regulator in the glaze, which contains approximately 3 wt% CuO. Therefore, in this structure, the Pb^{2+} in the green glaze readily undergoes ion exchange or hydrolysis reactions in the water and dissolves. The dissolved Pb^{2+} reacts with anions in the ocean to form insoluble deposits of PbS, $PbSO_4$, and $PbCO_3$. The shipwreck contains many Fe and Cu artifacts that corrode easily in the presence of sulfate-reducing bacteria to produce metal sulfides [67], which are the sources of minerals trapped in the corrosion layer of the Pb glaze, such as pyrite, chalcopyrite, and covellite.

As a result of the lack of O_2 in the seabed silt environment, Fe mainly occurs in the form of ferro sulfide compounds, such as pyrite and chalcopyrite. The unearthed samples were placed in deionized water for desalination treatment, at which time the solution was high in O_2. Due to the lattice defects in pyrite and the presence of dissociation planes, pyrite easily undergoes oxidation reactions with O_2 and H_2O in the surrounding environment [68–70]. First, the surface is oxidized to release small quantities of H^+, Fe^{2+}, and SO_4^{2-} (Eq. 2). Then, Fe^{2+} is oxidized by O_2 in the air

to form Fe^{3+} (Eq. 3). The generated Fe^{3+} is very likely to oxidize pyrite to produce large quantities of Fe^{2+} and SO_4^{2-} (Eq. 4). The generated Fe^{2+} is reoxidized to Fe^{3+} by O_2 (Eq. 3). These three reactions cycle until the pyrite is completely oxidized. When pyrite leaves the humid environment, the iron oxyhydroxide loses H_2O to form iron oxide (Eq. 5). In addition to chemical oxidation, pyrite also undergoes biological oxidation by S-oxidizing bacteria, such as *Thiobacillus ferrooxidans* and *Thiobacillus thiooxidans* [71]. Therefore, the iron oxide layer formed on the surface of the N4 sample resulted from changes in the environment used to store the samples after they were unearthed.

$$2FeS_2 + 7O_2 + 2H_2O \longrightarrow 2Fe^{2+} + 4H^+ + 4SO_4^{2-} \quad (2)$$

$$4Fe^{2+} + O_2 + 4H^+ \longrightarrow 4Fe^{3+} + 2H_2O \quad (3)$$

$$FeS_2 + 14Fe^{3+} + 8H_2O \longrightarrow 15Fe^{2+} + 2SO_4^{2-} + 16H^+ \quad (4)$$

$$2Fe(OH)_3 \longrightarrow Fe_2O_3 + 3H_2O \quad (5)$$

Pyrite is easily oxidized in a humid environment to generate sulfuric acid (H_2SO_4) that increases the acidity of the solution, which in turn can accelerate the corrosion of the glaze layer. After oxidation, the pyrite can form hydrated iron sulfate, which has a higher unit molecular volume. The loss of H_2O and subsequent precipitation leave the glaze susceptible to stress damage. Therefore, reducing the activities of metal sulfides, such as pyrite, in the corrosion of the Pb glaze layer is an important research topic.

Corrosion mechanism of lead glaze

The Pb glaze is structurally similar to alkali silicate glass and thus has a similar corrosion mechanism. In studies of glass corrosion mechanisms, a gel layer is often considered to result from solid-state recondensation of a residual partially hydrolyzed glass network produced by diffusion-controlled ion exchange and hydration reactions. Observation of the composition and morphology of the corrosion layer on the surface of the unearthed Pb-glazed pottery (which has remained in seawater for more than 800 years) showed the following main characteristics: (1) alternating deposition of Si- and Pb-rich layers; (2) a sharp change in the Si content at the interface between the Si-rich layer and the pristine glass, which formed a sharp interface; (3) the Si-rich layer contains agglomerates of spherical particles and is highly porous. Thus, the corrosion on the surface of the Pb glaze described in this study clearly cannot be explained by the residual hydrated glass model, but the "interface-coupled dissolution–precipitation (ICDP)" mechanism is more suitable in explaining the corrosion process of the samples investigated in this study.

The seawater around the shipwreck is weakly alkaline and has a salinity of 30.6‰. For the Pb glaze immersed in seawater, the orthosilicic acid (H_4SiO_4) in the solution on the glaze surface is undersaturated. Thus, the Pb glaze first dissolves congruently, the silicone skeleton in the lead glaze is gradually hydrolyzed, and H_4SiO_4 are released into the solution. At the same time, Pb^{2+}, the network-modifying ion in the glaze, is also released into the solution. As Pb^{2+} modifies the silicate network and easily leaches into solution, diffusion-controlled proton-cation exchange may precede congruent dissolution–precipitation of the glass. However, the congruent dissolution–precipitation rate of the glass exceeds the diffusion rate, thus controlling the overall corrosion rate (Fig. 13a). As the concentration of H_4SiO_4 increases, individual H_4SiO_4 are polymerized together in solution by a condensation reaction. In the solution boundary layer near the glaze surface, the supersa turated H_4SiO_4 preferentially nucleate through polycondensation at the hydroxylation sites on the surface of the dissolved glass. For the large spherical hydrated silica particles, the H_4SiO_4 around the nucleus then continues to grow by polymerization. The Si-rich layer of the sample is a random accumulation of spherical hydrated silica colloidal particles with diameters of 50–150 nm, where the pores in the layer correspond to gaps between the particles and are not formed by ion exchange and solid-state reorganization in the residual glass. Since thermodynamic equilibrium between the glass and the solution cannot be reached, if the solution reach the surface of the glaze through the Si-rich gel pores, congruent glass dissolution can continue to occur, providing an interfacial solution with orthosilicates. As a result, an increasing number of Si-rich layers can grow inward to replace the pristine glaze. The pore properties (e.g., the pore size and connectivity) affect the transport of species from the solution to the reaction interface, thereby controlling the kinetics of the reaction. The Pb^{2+} leach via congruent dissolution is relatively soluble in the solution, and Pb^{2+} in the solution diffuses readily and has a wider migration range than the SiO_2 gel. Therefore, the SiO_2 colloids first precipitate at the reaction interface, and then Pb^{2+} reacts with the S^{2-}, SO_4^{2-}, and CO_3^{2-} in the solution at the reaction interface to form insoluble compounds that are deposited on the Si-rich gel layer. S^{2-} has the smallest volume among the ions and easily enters the innermost layer through the pores to generate PbS during the inward corrosion process (Fig. 13b, c). Increases in both the degree of polymerization of the gel layer and the number of corrosion

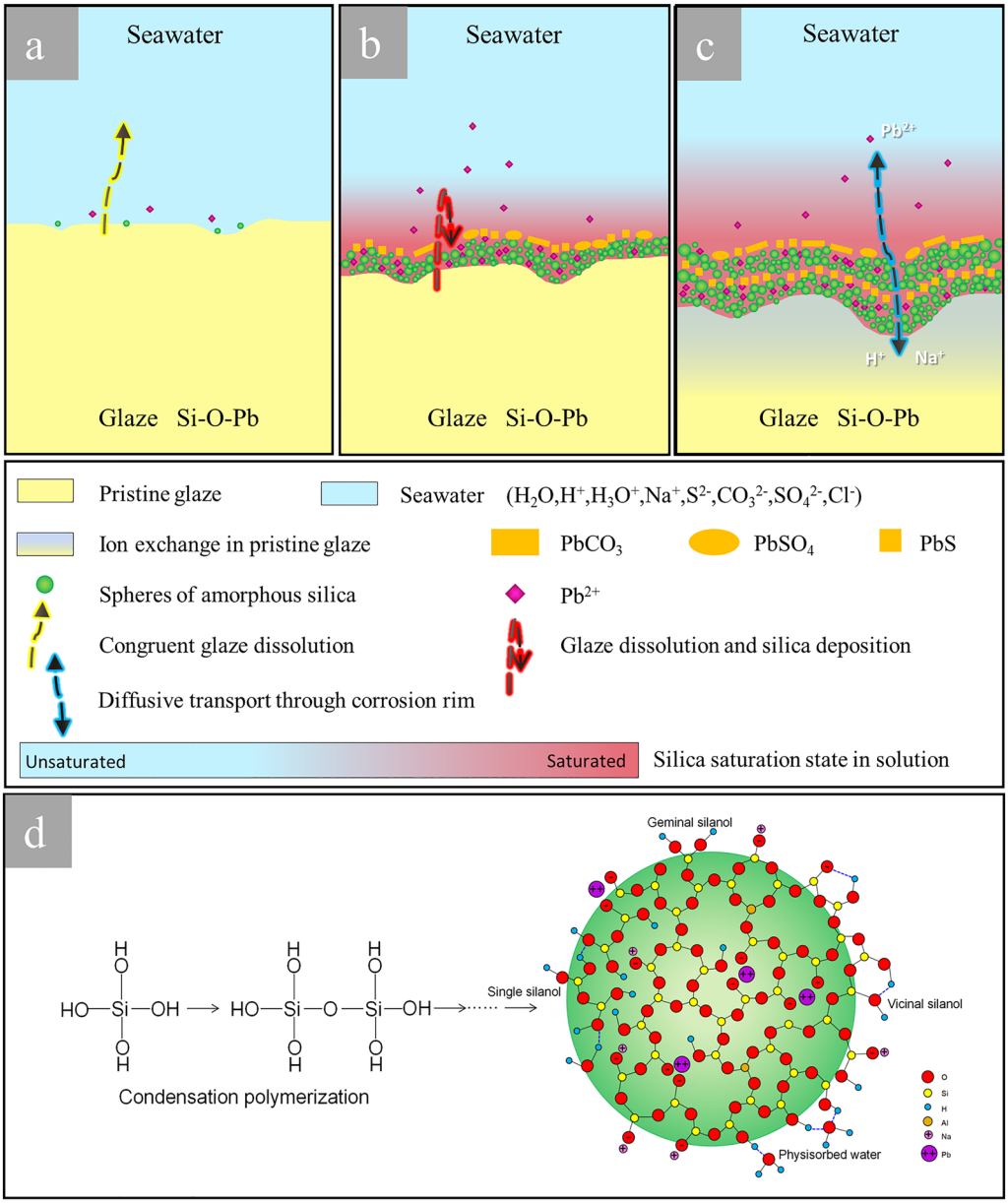

Fig. 13 Schematic diagram. **a–c** Glaze corrosion process; **d** Formation process of spherical SiO_2 colloidal particles

layers inhibits the transport of dissolved substances between the water and glaze, and the congruent dissolution rate decreases. At this time, diffusion-controlled ion exchange and hydration layers start to appear in the corroded glaze at the reaction front, and an approximately 500 nm-thick ion diffusion layer and an approximately 700 nm-thick hydration layer are visible on the element line distribution map of the N4 sample (Figs. 11, 13c).

In alkaline solutions with pHs above 7, many ≡Si–O^- groups form inside and on the surfaces of the spherical SiO_2 particles. Cationic Pb^{2+} leached from the glaze and cations with high concentrations in the marine solution, such as Na^+ and K^+, can be captured and adsorbed by ≡Si–O^-. As the polymerization degree increases, more elements are locked into the SiO_2 network, enriching the Si-rich layer with Pb, Na, and K. The dissolved Al ions in the glaze replace Si and become embedded in the skeleton. The dissolved ions in the glaze may also react with the ions in solution to form precipitates and accumulate in the gel pores (Fig. 13d). Despite the desalination and soaking treatment, the Si-rich layer still has high concentrations of cations, which indirectly

indicates that the corresponding elements are adsorbed in the gel network through chemical bonding.

In the marine environment, the temperature changes are small, but the pH and electrolyte concentration can fluctuate due to various local chemical reactions, renewal of the marine solution, and the action of microorganisms. For example, in an alkaline environment, dehydration and polymerization of hydrated silica can release Na^+ and hydroxide (OH^-), increasing the pH and cation concentration of the solution. The formation of PbS and $PbCO_3$ precipitates can promote ionization of the local weak acid and reduce the pH and concentration of cations. The attachment of marine microorganisms also releases organic acids locally [72, 73]. The dissolution rate of glass and the solubility, dissolution rate, and precipitation rate of the amorphous silica in the corrosion layer are all affected by the pH of the interfacial solution and the electrolyte concentration (the ionic strength) [74–78]. Even small changes in the properties of the interfacial solution can affect the microstructure of the Si-rich gel layer. Fluctuations in the properties of the reacting solution at the interface may explain the formation of multiple corrosion layers on the glaze.

Conclusion

For the remnants of the green-glazed pottery found in the "Nanhai I" shipwreck, the glaze is a low-temperature SiO_2-Al_2O_3-PbO glaze, with Pb^{2+} as the main flux and Cu^{2+} as the main colorant. The corrosion products on the green glaze surface are distributed in alternating Si- and Pb-rich layers. The Si-rich layer is mainly formed by the random accumulation of silica spherical particles. The Pb-rich layer mainly contains galena (PbS), anglesite ($PbSO_4$), and cerussite ($PbCO_3$) crystals. In addition, covellite (CuS), pyrite (FeS_2), chalcopyrite ($CuFeS_2$), quartz, and small clay particles are attached to the glaze surface. The black area of the sample has a high galena content, and the golden yellow area contains hematite and spherical pyrite, which explains why this area appears black and gold.

The microscopic characteristics of the glaze corrosion layer, such as a sharp reaction boundary, high porosity, and a gel formed by the accumulation of spherical particles can be attributed to a coupled dissolution-reprecipitation mechanism. The corrosion layer does not form by interdiffusion but is precipitated directly from seawater by the stoichiometric dissolution of glass, that is, by congruent dissolution rather than selective dissolution. Ion exchange occurs during the corrosion process but is not the main rate-limiting process because the coupled dissolution–precipitation rate of the glaze exceeds the ion exchange rate. As the thickness of the gel layer increases, material transport is hindered, and the dissolution reaction of the glaze slows. At this time, diffusion-controlled ion exchange and hydration reactions begin to expose. Modern analytical techniques were used to investigate the corrosion process and mechanism for ancient lead glaze samples in this study. In future studies, simulation experiments will be performed to investigate the corrosion mechanisms of such samples further.

Supplementary Information

The online version contains supplementary material available at https://doi.org/10.1186/s40494-023-00965-w.

Additional file 1. Fig. S1. SEM images of the golden yellow area surface. **Fig. S2**. SEM images of the polished cross-section of golden yellow crust area. **Fig. S3**. SEM images of the surface iridescent area. Fig. S4. SEM images of the black crust area surface. **Fig. S5**. SEM images of the polished crosssection of black crust area. **Fig. S6**. Polarized light optical micrographs of the polished crosssection of black crust area. **Table S1**. EDS analysis results of the positions marked in **Fig.S1** (Wt%). **Table S2**. EDS analysis results of the positions marked in Fig.S2 (Wt%). **Table S3**. EDS analysis results of the positions marked in **Fig.S3** (Wt%). **Table S4**. EDS analysis results of the positions marked in **Fig.S4** (Wt%). **Table S5**. EDS analysis results of the positions marked in **Fig.5** (Wt%).

Acknowledgements

The authors would like to express their great gratitude to Mr. Yunpeng Wang from the Shandong Cultural Relics Conservation and Restoration Center, and associate professor Shuqiang Xu, Ms. Qi Jiang, from Shandong University for their help in experiments testing, and Dr. Yongdong Tong from University of Science and Technology Beijing for revision of the manuscript.

Author contributions

QM & ZL provided support and guidance for this study; BZ performed all experiments test, interpreted the data and wrote the manuscript; ZZ assisted with the majority of the measurements and analyses, revised manuscript; NL provided the samples and assistance in the study. All authors read and approved the final manuscript.

Funding

This research is funded by China's National Key R&D Program (2020YFC1521802).

Availability of data and materials

Not applicable.

Declarations

Competing interests

The authors declare that they have no competing interests.

Received: 14 February 2023 Accepted: 2 June 2023
Published online: 23 June 2023

References

1. Guangdong Institute of Cultural Relics and Archaeology, State Administration of Cultural Heritage Protection Center for Underwater Cultural Heritage. 2022. Underwater Archaeology Project of the Southern Song Dynasty Shipwreck "Nanhai I" in Guangdong. http://www.ncha.gov.cn/art/2022/5/26/art_2619_174549.html. Accessed 26 May 2022.
2. State Administration of Cultural Heritage Protection Center for Underwater Cultural Heritage, National Museum of China, Guangdong Provincial

Institute of Cultural Relics and Archaeology, Yangjiang City Museum. One of the archaeological reports of the "Nanhai I" shipwreck-1989–2004 survey. Beijing: Cultural relics press; 2017. ISBN:9787501053278.
3. Lang J, Cui J. The style and origin of glazed pottery lei unearthed from the Qi tomb of the Warring States period in Linzi: a discussion on the origin of lead glazed pottery in China. Huaxia Archaeol. 2017;02:95–101. https://doi.org/10.16143/j.cnki.1001-9928.2017.02.009.
4. Li G, Guo Y. Technological bases of famous Chinese porcelains. Hangzhou: Zhejiang University Press; 2012.
5. Luo D, Zheng J. New archaeological progress in lead glazed pottery kiln sites from the Han Dynasty to the Southern and Northern Dynasties since the 21st century. Cultural Relics World. 2022;09:112–8.
6. Laufer B. Chinese Pottery of the Han Dynasty, Reprinted in Tientsin, China. 1940th ed. Leiden: E. J. Brill Ltd.; 1909.
7. Hobson RL. Glazed han pottery. Trans Orient Ceram Soc. 1925;5:21–5.
8. Jackson H. The iridescence on early Chinese lead glazes. Trans Orient Ceram Soc. 1924;4:13–23.
9. Naito T. The new edition of the science of ancient ceramics. Tokyo: Yuzankaku Shuppan; 1964.
10. Ye Z. Elementary Introduction to the ancient Chinese pottery. Beijing: China Light Industry Press; 1982.
11. Zhang F, Zhang Z. Low-temperature coloured glazes of succesive dynasties in ancient China. J Chin Ceramic Soc. 1980. https://doi.org/10.14062/j.issn.0454-5648.1980.01.002.
12. Wood N, Watt J, Kerr R, Brodrick A, Darrah J. An examination of some Han dynasty lead glazed wares. Sci Technol Ancient Ceram. 1992:29–142.
13. Zhu T, Wang C, Mao Z, Li L, Huang H. Identification of different corrosion covering the surface of Chinese ancient lead glazed potteries. Spectrosc Spectral Anal. 2010;30(01):266–9. https://doi.org/10.3964/j.issn.1000-0593(2010)01-0266-04.
14. Lu X, Li W, Luo H. Characteristics and source analysis on the ceramic wares unearthed from the emperor tombs of the Southern Han kingdom in Five Dynasties. J Chin Ceramic Soc. 2011;39(05):818–24. https://doi.org/10.14062/j.issn.0454-5648.2011.05.009.
15. Hui R, Wang L, Lu Z, Yang Z. Study on white corrosion of ancient glazed structural components of Shanshan guild hall in Luoyang. Archaeol Cultural Relics. 2013;6:105–8. https://doi.org/10.3969/j.issn.1000-7830.2013.06.015.
16. Zhao J, Wang L, Luo H, Li W, Li X. Analysis of the main deterioration products of glazed tiles excavated from the site of Bao'en Temple in Nanjing, China. J Nanjing Univ (Natural Sciences). 2014;50(01):95–102. https://doi.org/10.13232/j.cnki.jnju.2014.01.014.
17. He Q, Lv S, Pei Y, Li Y, Zhao R. Formation and analysis of corrosion products on green yellow glazed pottery from the Caocun kiln. Sci Conserv Archaeol. 2014;26(02):16–21. https://doi.org/10.16334/j.cnki.cn31-1652/k.2014.02.006.
18. Garofano I, Robador MD, Perez-Rodriguez JL, Castaing J, Pacheco C, Duran A. Ceramics from the Alcazar Palace in Seville (Spain) dated between the 11th and 15th centuries: compositions, technological features and degradation processes. J Eur Ceram Soc. 2015;35(15):4307–19. https://doi.org/10.1016/j.jeurceramsoc.2015.07.033.
19. Giannossa LC, Fico D, Pennetta A, Mangone A, Laviano R, De Benedetto G. Integrated investigations for the characterisation of Roman lead-glazed pottery from Pompeii and Herculaneum (Italy). Chem Pap. 2015;69(8):1033–43. https://doi.org/10.1515/chempap-2015-0110.
20. Yin X, Huang TJ, Gong H. Chemical evolution of lead in ancient artifacts—a case study of early Chinese lead-silicate glaze. J Eur Ceram Soc. 2020;40(5):2222–8. https://doi.org/10.1016/j.jeurceramsoc.2020.01.002.
21. Laubengayer AW. The weathering and iridescence of some ancient roman glass found in Cyprus. J Am Ceram Soc. 1931;14:833–6. https://doi.org/10.1111/j.1151-2916.1931.tb16577.x.
22. Cox GA, Ford BA. The long-term corrosion of glass by ground-water. J Mater Sci. 1993;28:5637–47. https://doi.org/10.1007/BF00367840.
23. Emami M, Nekouei S, Ahmadi H, Pritzel C, Trettin R. Iridescence in ancient glass: a morphological and chemical investigation. Int J Appl Glass Sci. 2016;7:59–68. https://doi.org/10.1111/ijag.12182.
24. Gueli AM, Pasquale S, Tanasi D, Hassam S, Lemasson Q, Moignard B, Pacheco C, Pichon L, Stella G, Politi G. Weathering and deterioration of archeological glasses from late Roman Sicily. Int J Appl Glass Sci. 2020;11:215–25. https://doi.org/10.1111/ijag.14076.
25. Verney-Carron A, Gin S, Libourel G. A fractured roman glass block altered for 1800 years in seawater: analogy with nuclear waste glass in a deep geological repository. Geochim Cosmochim Ac. 2008;72(22):5372–85. https://doi.org/10.1016/j.gca.2008.08.018.
26. Dal Bianco B, Bertoncello R, Milanese L, Barison S. Glass corrosion across the Alps: a surface study of chemical corrosion of glasses found in marine and ground environments. Archaeometry. 2005;47:351–60. https://doi.org/10.1111/j.1475-4754.2005.00206.x.
27. Silvestri A, Molin G, Salviulo G. Archaeological glass alteration products in marine and land-based environments: morphological, chemical and microtextural characterization. J Non-Cryst Solids. 2005;351(16–17):1338–49. https://doi.org/10.1016/j.jnoncrysol.2005.03.013.
28. Silvestri A, Viti C, Molin G, Salviulo G. From Micro- to Nano-arrangement: alteration products in archaeological glass from marine and land-based environments. In: Turbanti-Memmi, I. (eds) Proceedings of the 37th International Symposium on Archaeometry, 13th-16th May 2008, Siena, Italy. Springer, Berlin, Heidelberg. 2011. https://doi.org/10.1007/978-3-642-14678-7_55.
29. Anaf W. Study on the formation of heterogeneous structures in leached layers during the corrosion process of glass. CeROArt: Conservation, Exposition, Restauration d'Objets d'Art. 2010; 6:2–14.
30. Dohmen L, Lenting C, Fonseca ROC, Nagel T, Heuser A, Geisler T, Denkler R. Pattern formation in silicate glass corrosion zones. Int J Appl Glass Sci. 2013;4:357–70. https://doi.org/10.1111/ijag.12046.
31. Doremus RH. Interdiffusion of hydrogen and alkali ions in a glass surface. J Non-Cryst Solids. 1975;19:137–44. https://doi.org/10.1016/0022-3093(75)90079-4.
32. Bunker BC. Molecular mechanisms for corrosion of silica and silicate glasses. J Non-Cryst Solids. 1994;179:300–8. https://doi.org/10.1016/0022-3093(94)90708-0.
33. Cailleteau C, Angeli F, Devreux F, Gin S, Jestin J, Jollivet P, Spalla O. Insight into silicate-glass corrosion mechanisms. Nat Mater. 2008;7(12):978–83. https://doi.org/10.1038/nmat2301.
34. Frugier P, Gin S, Minet Y, Chave T, Bonin B, Godon N, Lartigue JE, Jollivet P, Ayral A, De Windt L, Santarini G. SON68 nuclear glass dissolution kinetics: current state of knowledge and basis of the new GRAAL model. J Nucl Mater. 2008;380(1–3):8–21. https://doi.org/10.1016/j.jnucmat.2008.06.044.
35. Bunker BC, Headley TJ, Douglas SC. Gel structures in leached alkali silicate glass. MRS Online Proc Libr. 1984;32(1):41. https://doi.org/10.1557/PROC-32-41.
36. McGrail BP, Icenhower JP, Shuh DK, Liu P, Darab JG, Baer DR, Thevuthasen S, Shutthanandan V, Engelhard MH, Booth CH, Nachimuthu P. The structure of Na2O-Al2O3-SiO2 glass: impact on sodium ion exchange in H2O and D2O. J Non-Cryst Solids. 2001;296(1–2):10–26. https://doi.org/10.1016/S0022-3093(01)00890-0.
37. Gin S, Jollivet P, Fournier M, Angeli F, Frugier P, Charpentier T. Origin and consequences of silicate glass passivation by surface layers. Nat Commun. 2015;6:6360. https://doi.org/10.1038/ncomms7360.
38. Gin S, Collin M, Jollivet P, Fournier M, Minet Y, Dupuy L, Mahadevan T, Kerisit S, Du J. Dynamics of self-reorganization explains passivation of silicate glasses. Nat Commun. 2018;9:2169. https://doi.org/10.1038/s41467-018-04511-2.
39. Gin S, Ryan JV, Schreiber DK, Neeway J, Cabié M. Contribution of atom-probe tomography to a better understanding of glass alteration mechanisms: application to a nuclear glass specimen altered 25years in a granitic environment. Chem Geol. 2013;349–350:99–109. https://doi.org/10.1016/j.chemgeo.2013.04.001.
40. Hellmann R, Cotte S, Cadel E, Malladi S, Karlsson LS, Lozano-Perez S, Cabié M, Seyeux A. Nanometre-scale evidence for interfacial dissolution-reprecipitation control of silicate glass corrosion. Nature Mater. 2015;14(3):307–11. https://doi.org/10.1038/nmat4172.
41. Putnis A. Sharpened interface. Nat Mater. 2015;14:261–2. https://doi.org/10.1038/nmat4198.
42. Gin S, Jollivet P, Barba Rossa G, Tribet M, Mougnaud S, Collin M, Fournier M, Cadel E, Cabie M, Dupuy L. Atom-Probe Tomography, TEM and ToF-SIMS study of borosilicate glass alteration rim: a multiscale approach to investigating rate-limiting mechanisms. Geochim Cosmochim Ac. 2017;202:57–76. https://doi.org/10.1016/j.gca.2016.12.029.
43. Geisler T, Janssen A, Scheiter D, Stephan T, Berndt J, Putnis A. Aqueous corrosion of borosilicate glass under acidic conditions: a new corrosion

mechanism. J Non-Cryst Solids. 2010;356(28–30):1458–65. https://doi.org/10.1016/j.jnoncrysol.2010.04.033.
44. Geisler T, Nagel T, Kilburn MR, Janssen A, Icenhower JP, Fonseca ROC, Grange M, Nemchin AA. The mechanism of borosilicate glass corrosion revisited. Geochim Cosmochim Ac. 2015;158:112–29. https://doi.org/10.1016/j.gca.2015.02.039.
45. Lenting C, Plümper O, Kilburn MR, Guagliardo P, Klinkenberg M, Geisler T. Towards a unifying mechanistic model for silicate glass corrosion. npj Mater Degrad. 2018;2:1–10. https://doi.org/10.1038/s41529-018-0048-z.
46. Putnis A. Mineral replacement reactions: from macroscopic observations to microscopic mechanisms. Mineral Mag. 2002;66(5):689–708. https://doi.org/10.1180/0026461026650056.
47. Putnis CV, Ruiz-Agudo E. The mineral-water interface: where minerals react with the environment. Elements. 2013;9(3):177–82. https://doi.org/10.2113/gselements.9.3.177.
48. Putnis A. Why mineral interfaces matter. Science. 2014;343:1441–2. https://doi.org/10.1126/science.1250884.
49. Automatic intelligent background removal. https://www.renishaw.com/en/automatic-intelligent-background-removal--25934.
50. "Nanhai I" archaeological team. The Excavation of the Shipwreck "Nanhai I" of the Song Dynasty in 2014. Archaeology. 2016;(12):56–83.
51. Furukawa T, Brawer SA, White WB. The structure of lead silicate glasses determined by vibrational spectroscopy. J Mater Sci. 1978;13(2):268–82. https://doi.org/10.1007/BF00647770.
52. Wang PW, Zhang L. Structural role of lead in lead silicate glasses derived from XPS spectra. J Non-Cryst Solids. 1996;194(1–2):129–34. https://doi.org/10.1016/0022-3093(95)00471-8.
53. Fayon F, Bessada C, Massiot D, Farnan I, Coutures JP. 29Si and 207Pb NMR study of local order in lead silicate glasses. J Non-Cryst Solids. 1998;232–234:403–8. https://doi.org/10.1016/S0022-3093(98)00470-0.
54. Wu D, Jiang B, Lv Y, Wei H, Guo Y, Jiao S. The Relationships in the lead-release and other element-releases of the Chinese powder doped colours—with a Discussion on the mechanizm of lead-release. China ceramics. 1990. https://doi.org/10.16521/j.cnki.issn.1001-9642.1990.05.002.
55. Wu D, Wang F, Jiang Z, Jiao S, Wei H, Guo Y. Spectral characteristics of powder doped color (Feichui) and coloration mechanizm. China Ceramics. 1989. https://doi.org/10.16521/j.cnki.issn.1001-9642.1989.04.001.
56. Vilarigues M, da Silva RC. The effect of Mn, Fe and Cu ions on potash-glass corrosion. J Non-Cryst Solids. 2009;355(31–33):1630–7. https://doi.org/10.1016/j.jnoncrysol.2009.05.051.
57. Cvejic Z, Rakic S, Kremenovic A, Antic B, Jovalekic C, Colomban P. Nanosize ferrites obtained by ball milling: Crystal structure, cation distribution, size-strain analysis and Raman investigations. Solid State Sci. 2006;8(8):908–15. https://doi.org/10.1016/j.solidstatesciences.2006.02.041.
58. Jacquemin M, Simon P, Canizares A, Hennet L, Bessada C, Skrelic D, Gouillart E, Burov E. High-sensitivity Raman imaging of the surface of casted glass plates. J Raman Spectrosc. 2021;52:1048–54. https://doi.org/10.1002/jrs.6086.
59. Colomban P. Polymerization degree and Raman identification of ancient glasses used for jewelry, ceramic enamels and mosaics. J Non-Cryst Solids. 2003;323(1–3):180–7. https://doi.org/10.1016/S0022-3093(03)00303-X.
60. Colomban P, Paulsen O. Non-destructive determination of the structure and composition of glazes by Raman spectroscopy. J Am Ceram Soc. 2005;88:390–5. https://doi.org/10.1111/j.1551-2916.2005.00096.x.
61. Kacem IB, Gautron L, Coillot D, Neuville DR. Structure and properties of lead silicate glasses and melts. Chem Geol. 2017;461:104–14. https://doi.org/10.1016/j.chemgeo.2017.03.030.
62. Feller S, Lodden G, Riley A, Edwards T, Croskrey J, Schue A, Liss D, Stentz D, Blair S, Kelley M, Smith G, Singleton S, Affatigato M, Holland D, Smith ME, Kamitsos EI, Varsamis CPE, Ioannou E. A multispectroscopic structural study of lead silicate glasses over an extended range of compositions. J Non-Cryst Solids. 2010;356(6–8):304–13. https://doi.org/10.1016/j.jnoncrysol.2009.12.003.
63. Guangdong provincial chronicle compilation committee, Guangdong provincial chronicle · ocean and island. Guangzhou:Guangdong people's publishing house; 2000.
64. Lin J, Wang Y, Wang C, Ye S, Wang S. Chemistry and formation-evolution pattern of ooze water in the north of Nanhai sea. Geosci. 1994;8(1):107–18.
65. Schulz HD, Zable M. Marine Ceochemistry. 2nd ed. Berlin Heidelberg: Springer; 2006.
66. Shen D. Sulfur and iron compounds in marine excavated wood artifacts. Beijing: Science Press; 2020.
67. Tian X. Corrosion and protection of copper wares excavated from the sea. Beijing: Cultural Relics Press; 2019.
68. Chandra AP, Gerson AR. The mechanisms of pyrite oxidation and leaching: a fundamental perspective. Surf Sci Rep. 2010;65(9):293–315. https://doi.org/10.1016/j.surfrep.2010.08.003.
69. Murphy R, Strongin DR. Surface reactivity of pyrite and related sulfides. Surf Sci Rep. 2009;64(1):1–45. https://doi.org/10.1016/j.surfrep.2008.09.002.
70. Buckley AN, Woods R. The surface oxidation of pyrite. Appl Surf Sci. 1987;27(4):437–52. https://doi.org/10.1016/0169-4332(87)90153-X.
71. Sand W, Gehrke T, Jozsa PG, Schippers A. (Bio)chemistry of bacterial leaching—direct vs. indirect bioleaching. Hydrometallurgy. 2001;59(2–3):159–75. https://doi.org/10.1016/S0304-386X(00)00180-8.
72. Imo EO, Ihejirika CE, Orji JC, Nweke CO, Adieze IE. Mechanism of microbial corrosion: a review. J Chem Bio Phys Sci Sec B. 2016;6(4):1173–8.
73. Loto CA. Microbiological corrosion: mechanism, control and impact-a review. Int J Adv Manuf Technol. 2017;92:4241–52. https://doi.org/10.1007/s00170-017-0494-8.
74. Iler RK. The chemistry of silica: solubility, polymerization, colloid and surface properties and biochemistry of silica. USA: John Wiley & Sons; 1979. p. 3–104.
75. Icenhower JP, Dove PM. The dissolution kinetics of amorphous silica into sodium chloride solutions: effects of temperature and ionic strength. Geochim Cosmochim Ac. 2000;64(24):4193–203. https://doi.org/10.1016/S0016-7037(00)00487-7.
76. Conrad CF, Icopini GA, Yasuhara H, Bandstra JZ, Brantley SL, Heaney PJ. Modeling the kinetics of silica nanocolloid formation and precipitation in geologically relevant aqueous solutions. Geochim Cosmochim Ac. 2007;71(3):531–42. https://doi.org/10.1016/j.gca.2006.10.001.
77. Rimstidt JD, Zhang Y, Zhu C. Rate equations for sodium catalyzed amorphous silica dissolution. Geochim Cosmochim Acta. 2016;195:120–5. https://doi.org/10.1016/j.gca.2016.09.020.
78. Wang Y, Jove-Colon CF, Lenting C, Icenhower JP, Kuhlman KL. Morphological instability of aqueous dissolution of silicate glasses and minerals. npj Mater Degrad. 2018;2:1–10. https://doi.org/10.1038/s41529-018-0047-0.

Publisher's Note